Applied Nanoscience (2020) 10:4971–4976
https://doi.org/10.1007/s13204-020-01327-9

ORIGINAL ARTICLE

Nano-size defect layers in arsenic-implanted and annealed HgCdTe epitaxial films studied with transmission electron microscopy

O. Yu. Bonchyk[1] · H. V. Savytskyy[1] · I. I. Izhnin[2,3] · K. D. Mynbaev[4] · I. I. Syvorotka[2] · A. G. Korotaev[3] · A. V. Voitsekhovskii[3] · O. I. Fitsych[5] · V. S. Varavin[6] · D. V. Marin[6] · N. N. Mikhailov[3,6] · M. V. Yakushev[6] · Z. Swiatek[7] · J. Morgiel[7] · R. Jakiela[8]

Received: 6 December 2019 / Accepted: 25 February 2020 / Published online: 12 March 2020
© King Abdulaziz City for Science and Technology 2020

Abstract
Optical reflectance and bright-field and high-resolution transmission electron microscopy studies of radiation damage induced by implantation of arsenic ions with 190 keV and 350 keV energy and 10^{14} cm^{-2} fluence in molecular-beam epitaxy-grown $Hg_{0.7}Cd_{0.3}Te$ films were performed. A similarity in defect pattern formed by arsenic implantation in $Hg_{1-x}Cd_xTe$ with $x \approx 0.2$ and $x \approx 0.3$ straight after the implantation was observed with formation of three nano-size defect layers containing dislocation loops of vacancy- and interstitial-types, single dislocations and lattice deformations. After post-implantation arsenic activation annealing, most of these defects in our $Hg_{0.7}Cd_{0.3}Te$ films, in contrast to $Hg_{0.8}Cd_{0.2}Te$ films, disappeared. This effect is explained by the reduced influence of the electric field of the graded-gap surface layer on the diffusion of charged point defects under annealing.

Keyword HgCdTe · Arsenic implantation · Transmission electron microscopy · Defects

Background

$Hg_{1-x}Cd_xTe$ (MCT) is one of the most important materials for infrared (IR) photo-electronics, and MCT-based photodiodes are often fabricated with ex-situ formation of p–n junctions by ion implantation. Recently, there has been much interest in photodiode architecture based on arsenic implantation in n-type MCT base (Gravrand et al. 2009; Mollard et al. 2011; Park et al. 2016; Bazovkin et al. 2016; Bommena et al. 2015; Guinedor et al. 2019). Dark currents in p–n junctions of the p^+–n-type, which result from such implantation, are typically lower than those in n^+–p-type junctions, so a higher working temperature or longer wavelength cut-off sensitivity threshold of photodiodes can be achieved.

Since electrical properties of MCT straight after ion implantation are controlled by radiation defects rather than by the implanted species, a strong interest in the structural studies of arsenic-implanted MCT has been noted (Mollard et al. 2011; Lobre et al. 2014; Shi et al. 2016; Bonchyk et al. 2019). These studies are typically performed before and after activation annealing, whose task is to reduce the density of radiation defects and to achieve p^+-type doping via electrical activation of the implanted ions. Recently, we reported on the results of the transmission electron microscopy (TEM)

✉ O. Yu. Bonchyk
bonchyk@ukr.net

1 Ya.S. Pidstryhach Institute for Applied Problems of Mechanics and Mathematics NASU, Naukova 3b, Lviv 79060, Ukraine

2 Scientific Research Company "Electron-Carat", Stryiska 202, Lviv 79031, Ukraine

3 National Research Tomsk State University, Lenina 36, 634050 Tomsk, Russia

4 ITMO University, Kronverkskiy 49, 197101 Saint-Petersburg, Russia

5 Hetman Petro Sahaidachny National Army Academy, Gvardijska 32, Lviv 79012, Ukraine

6 A.V. Rzhanov Institute of Semiconductor Physics SB RAS, Ac. Lavrentieva 13, 630090 Novosibirsk, Russia

7 Institute of Metallurgy and Material Science PAN, Reymonta 25, 30-059 Krakow, Poland

8 Institute of Physics PAN, Al. Lotnikow 32/46, 02-668 Warsaw, Poland

studies of arsenic-implanted $Hg_{1-x}Cd_xTe$ films with the composition (CdTe molar fraction) $x=0.2$ (Bonchyk et al. 2019). These films are suitable for the fabrication of photodiodes operating in the long-wavelength (8–12 µm) IR range. Another important range that can be covered with MCT-based devices is the mid-wavelength IR (3–5 µm). Devices operating in this range require $Hg_{1-x}Cd_xTe$ with $x=0.3$, and due to the increased CdTe content this material should behave slightly differently under implantation than that with $x=0.2$. In this paper, we present the results of bright-field (BF−) and high-resolution (HR−) TEM studies of the microstructure of arsenic-implanted $Hg_{0.7}Cd_{0.3}Te$, both before and after activation annealing. Nano-size defect layers were revealed and identified in the implanted material and their evolution as a result of annealing was followed. The results of microscopy studies were compared to those of optical reflectance, which also allows for assessing the structural quality of the material.

Methods

HgCdTe films were grown by molecular-beam epitaxy (MBE) at A.V. Rzhanov Institute of Semiconductor Physics (Novosibirsk, Russia) on (013) CdTe/ZnTe/GaAs (sample 1) and CdTe/ZnTe/Si (sample 2) substrates with the growth cycle controlled in situ by means of an ellipsometer (Varavin et al. 2003; Yakushev et al. 2011). The 'absorber' layers of the films had constant composition $x=0.295\pm0.002$ for sample 1 and $x=0.297\pm0.003$ for sample 2. The films had graded-gap protective surface layers with composition at the surface approaching $x=0.60$ and thickness 0.5 µm (sample 1) and $x=0.45$ and thickness 0.3 µm (sample 2). The films were un-doped and after the growth, according to the results of the Hall-effect measurements performed at 77 K, they had n-type conductivity with electron concentration and mobility $\sim 1\cdot10^{14}$ cm^{-3} and $\mu_n \approx 45{,}000$ $cm^2/(V\cdot s)$, respectively. The total thickness of film 1 was 10.2 µm, that of film 2, 7.3 µm.

Samples cut from the as-grown films were implanted with As^+ ions with energies $E_{As}=190$ keV or $E_{As}=350$ keV with ion fluence 10^{14} cm^{-2}. The implantation was performed using IMC200 (Ion Beam Services, France) system. After the implantation, parts of the implanted samples were subjected to two-stage thermal activation annealing in saturated mercury vapors (360 °C, 2 h and 220 °C, 24 h). The first stage was performed to reduce the radiation damage and to activate the implanted arsenic, while the second stage was used to annihilate mercury vacancies generated during the growth, implantation, and the first annealing stage.

The microstructure observations were performed in BF-TEM and HRTEM modes using Tecnai G2 F20, FEI Company microscope. Thin foils for the observations were cut out using FEI Quanta 200 dual-beam focused ion (Ga^+) beam (FIB) machine equipped with Omniprobe™ lift-out system. The investigated material was first covered with 300 nm-thick amorphous carbon layer that prevented the surface from the damage which could be inflicted by Ga^+ ions used for the deposition of a Pt bar. Next, trench milling was done on both sides of the bar. Here, the effect of Ga^+ ions was minimized by limiting the gallium beam current during the milling, starting from 20 nA, continuing with 7 nA, and finishing with 5 nA. The final polishing of the lifted lamella was done starting from 1 nA ion beam current, continuing with 0.3 nA, and finishing with 0.1 nA. The energy of Ga^+ ions did not exceed 2 keV. The analysis of HRTEM images was carried out using direct and inverse fast Fourier transforms (FFT, IFFT). Reflectance spectra were recorded in 300–800 nm wavelength range with step 0.2 nm at $T=300$ K using Shimadzu UV-3600 (Japan) spectrometer.

Results

Figure 1 shows optical reflectance spectra for both samples implanted with $E_{As}=190$ keV and $E_{As}=350$ keV. As can be seen, increasing the implantation energy does not significantly change the shape of the spectra. It is known that a typical doublet of E_1 and $E_1+\Delta_1$ peaks exists in MCT reflectance spectra. These peaks are due to transitions $\Lambda_{4,5}\rightarrow\Lambda_6$ and $\Lambda_6\rightarrow\Lambda_6$, respectively. It is commonly accepted that the position of the peaks provides information on the energy gap (composition), while the shape of the peaks reflects structural perfection of the surface of the material (Koppel 1985). A useful method for quantitative assessment of the 'sharpness' of MCT reflectance peaks (and, therefore, surface structural quality) was proposed by Dvoretsky et al. (1998). In particular, to assess the change in the shape of the peaks after a treatment, the value of "peak sharpness" $Q=\Delta R/R_1$ can be used, where ΔR is the value of the 'dip' between the peaks and R_1 is the reflection in the maximum of the peak E_1. As can be seen, for the initial (before the implantation) sample 1 with the composition of the graded-gap layer at the surface $x_s=0.60$ peak E_1 is hardly seen. This contrasts the reflection spectra of this sample to that of sample 2 with the composition of the graded-gap layer $x_s=0.45$, where peak E_1 is clearly pronounced and has $Q=4.00$. Apparently this is indicative of much lower structural perfection of the surface of sample 1, most likely, in terms of compositional variations. For both films, after ion implantation peaks E_1 cannot be seen, which is indicative of strong implantation damage brought in as a result of the interaction of energetic ions with the surface. After activation annealing, peaks became much sharper, and for sample 2 the corresponding values of peak sharpness ($Q=4.51$ for $E_{As}=190$ keV and $Q=4.67$ for $E_{As}=350$ keV) substantially exceeded that measured for the

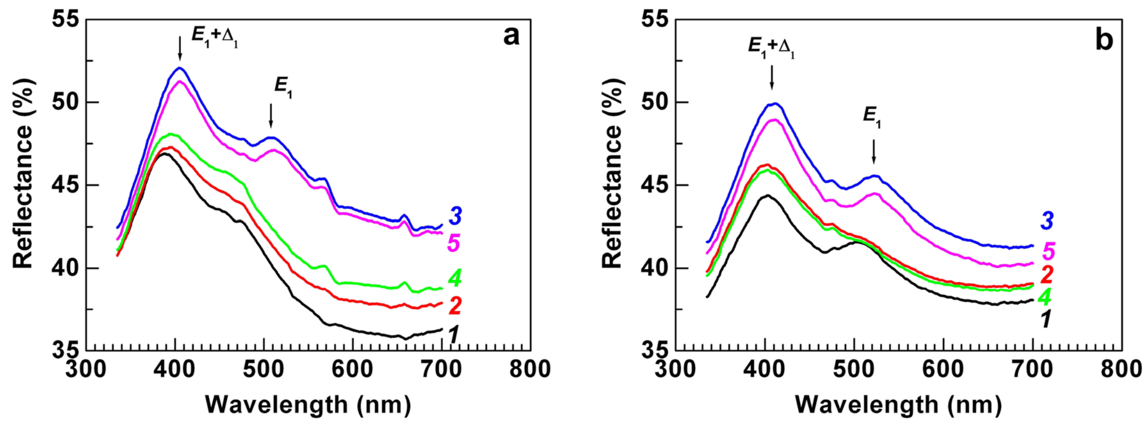

Fig. 1 Optical reflectance spectra for samples 1 (GaAs substrate) (**a**) and 2 (Si substrate) (**b**) recorded for as-grown films (curves 1), samples implanted with $E_{As}=190$ keV before (curves 2) and after (curves 3) activation annealing, and samples implanted with $E_{As}=350$ keV, also before (curves 4) and after (curves 5) annealing

initial sample. This was indicative of annihilation of structural defects formed under ion implantation. For sample 1, the corresponding values of peak sharpness after annealing comprised $Q=2.57$ after implantation with $E_{As}=190$ keV and $Q=2.92$ after implantation with $E_{As}=350$ keV.

Due to the higher structural quality of the surface of sample 2, as revealed by optical reflectance studies, we performed our TEM studies on this film. Figure 2a shows BF–TEM image of a cross-section of sample 2 before the implantation. A low density of small structural defects is observed; these defects are represented by dislocations, small (< 6 nm in linear size) dislocation loops, stacking faults and lattice deformations. It should be noted, that at the depths that exceeded a typical projected path of implanted ions in MCT (> 800 nm), one could observe more complex defect pattern. This can be seen in Fig. 2b, c, which show HRTEM data, namely, FFT—(b) and IFFT—processed (c) images of a typical defect structure in this area. The following defects can be seen there: a dislocation and a vacancy-type dislocation loop with linear size exceeding 6 nm (red arrows) and a neighbouring dislocation (object P_1), a small dislocation loop (P_2), and a stacking fault (P_3).

Figure 3 shows BF-TEM images of the cross-sections of sub-surface area of sample 2 straight after implantation with $E_{As}=190$ keV (a) and $E_{As}=350$ keV (b), as well as those of the corresponding samples subjected to activation annealing (c, d). Let us start with the result obtained after implantation with energy 190 keV (Fig. 3a). This material contains a considerable density of radiation-induced defects with the defect layer stretching down to the depth of 330 nm. The defect layer can be divided into three nano-size sub-layers. Sub-layer A has a thickness of 70 nm and has a low defect density. According to HRTEM data (images not shown), it contained only large isolated defects, such as dislocation loops with the linear size of 12 nm. The thickness of the next sub-layer B is 80 nm. It contains various defect complexes and small and large single defects, including large dislocation loops of both interstitial- and vacancy-types.

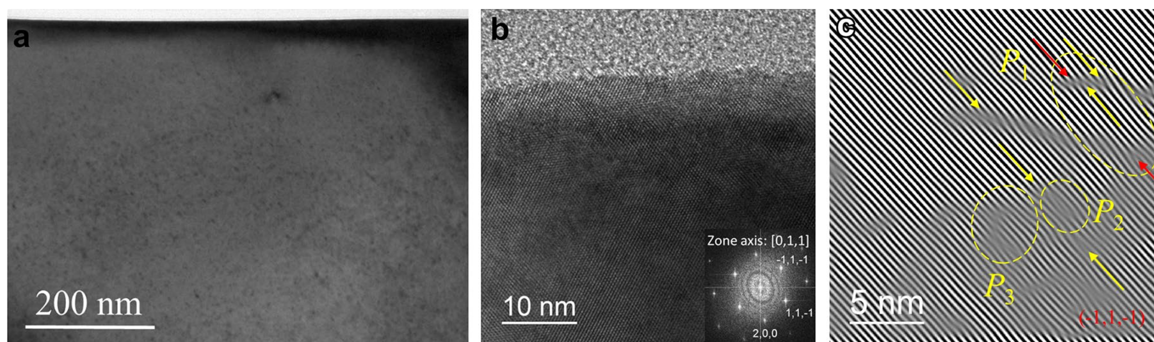

Fig. 2 Cross-sectional BF-TEM (**a**) and HRTEM (**b**) images of the sub-surface region of sample 2 before the implantation with inset showing a typical diffraction pattern of the defect area; image (**c**) shows an IFFT pattern of the image shown in the image (**b**). P_1, P_2 and P_3 objects are specific defects discussed in the text

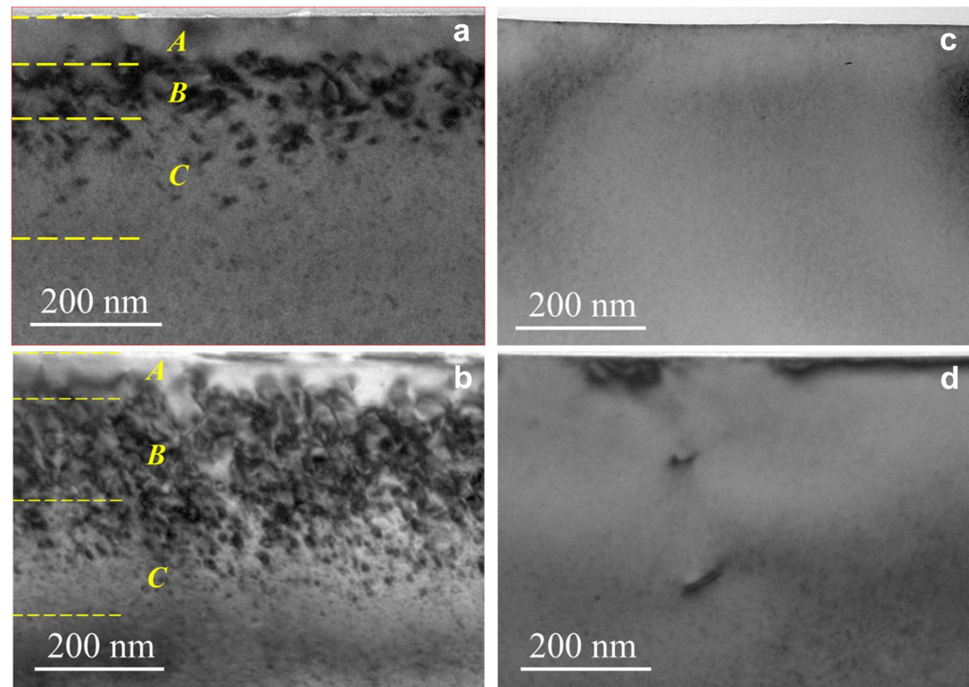

Fig. 3 Cross-sectional BF-TEM images of the sub-surface region of sample 2 straight after the implantation with arsenic ions with energy 190 keV (**a**) and 390 keV (**b**), and images taken after post-implantation activation annealing of the corresponding samples (**c**, **d**)

Small dislocation loops, typically of vacancy type, are also present there. When approaching the 'border' between this sub-layer and sub-layer C, the size of defects becomes smaller. In sub-layer C, whose thickness approaches 180 nm, one can observe gradual decrease in the size and density of defects. After activation annealing (Fig. 3c) the concentration of defects sharply decreases, for example, dislocation loops disappear completely. On the basis of HRTEM data (not shown) it was concluded that dominating defects in the annealed material were single dislocations, stacking faults and lattice deformations.

Sample 2 implanted with ions with 350 keV (Fig. 3b) had thicker defect layer (400 nm). This layer could also be divided into three nano-size sub-layers with different size and density of defects. Sub-layer *A* had low defect density and was 70 nm in thickness. Typical defects in this sub-layer, according to HRTEM data, were single dislocations, small (< 4 nm) dislocation loops, stacking faults and lattice deformations. Sub-layer B in this sample was much thicker than that in the sample implanted with $E_{As} = 190$ keV; its thickness equaled 155 nm. In this sub-layer, large (40 nm) dislocation loops were present along with single dislocations, stacking faults and lattice deformations. The thicknesses of sub-layers C in samples implanted with 190 and 350 keV energy were very similar and equaled 180 nm, and in both cases these sub-layers contained small dislocation loops, whose concentration was decreasing with the distance from the surface increasing.

After activation annealing of sample implanted with energy 350 keV (Fig. 3d) the concentration of defects sharply decreased. The dominating defects now were single dislocations and lattice deformations, which were located near the surface of the sample. The density of larger defects (such as dislocation loops with 6 nm in linear size, single dislocations and stacking faults) was low, and these defects were located at larger depths (in sub-layers B and C).

Figure 4 shows calculated (using SRIM package: www.srim.org) distributions of the implanted arsenic ions and the total number of generated vacancies against the background of selected fragments of the BF-TEM images of the cross-sections of sample 2. It can be seen that for both implantation energies the projected ion range R_P appears to lie within layer B, which has the highest concentration of extended defects. R_P is also close to the calculated maximum of arsenic concentration. In general, for both energies, the calculated profiles of implanted arsenic atoms appear to be in very good agreement with the defect density imaged in BF-TEM. In particular, the maximum depths at which structural defects are still can be seen in the images exactly correspond to the decrease observed on the defect profiles. With the energy of the implanted atoms increasing from 190 to 350 keV both the thickness of layer B and the full-width at half-maximum of the arsenic ion distribution curve increase. These results prove that the extended defects observed with TEM resulted from the direct effect of implanted ions rather from solid-state reactions that could be initiated by implantation. Let us note also that for both our samples the defect layers and arsenic distribution profiles were located within the graded-gap layers.

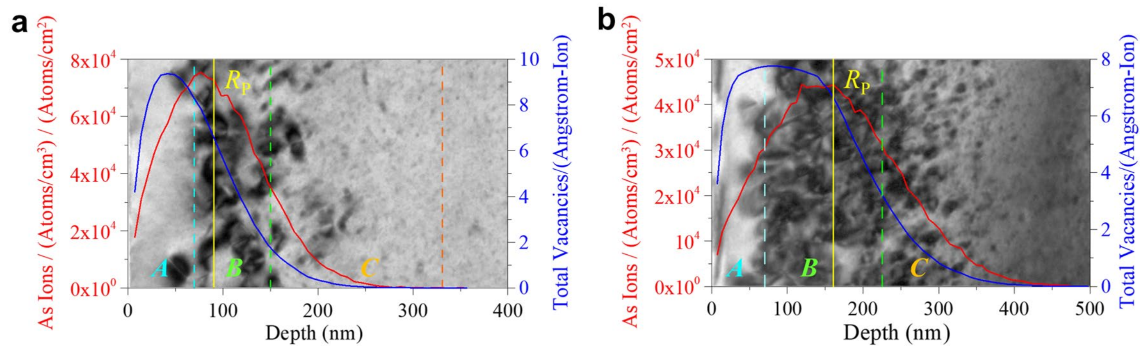

Fig. 4 Calculated (SRIM package) distributions of the implanted arsenic ions and the total number of vacancies against the background of selected fragments of the BF-TEM images of sample 2 implanted with arsenic ions with energy 190 keV (**a**) and 350 keV (**b**)

Discussion

Let us start the discussion with the comparison of the results of the studies of optical reflectance and those of TEM. The reflectance spectra showed that straight after the implantation the structural perfection of the surface seriously deteriorated, and the TEM data indeed confirmed the formation of extended defects in the sub-surface area of sample 2. The reflectance data obtained after activation annealing showed much higher value of Q than that after the growth, which was indicative of annihilation of sub-surface structural defects, and it also was confirmed by TEM. Let us note, though, that TEM data obtained after annealing of sample 2 implanted with $E_{As}=350$ keV showed the presence of single dislocations and lattice deformations near the surface (Fig. 3d), while the peak sharpness of the reflectance curve for this sample was high. This confirms that optical reflectance is not sensitive to the presence of single dislocations (Izhnin et al. 2019).

We should note also that the defect pattern obtained after activation annealing in this work was quite different from that which we earlier observed in arsenic-implanted and annealed MCT films with $x \approx 0.2$ (Izhnin et al. 2019). Straight after implantation the defect patterns with three nano-size sub-layers with different sizes and concentrations of defects in samples with $x \approx 0.2$ (Izhnin et al. 2019) and $x \approx 0.3$ (this work) were very similar. However, in samples with $x \approx 0.2$, a re-structuring of the defect structure of the radiation-damaged material during post-implantation annealing was observed and as a result of that, the 'defect' layer did not disappear but rather shifted towards the surface. In this work, we observed almost total annihilation of radiation-induced defects after post-implantation annealing rather than their re-structuring. A similar pattern of defect behaviour after post-implantation annealing was observed by Lobre et al. (2014) and Mollard et al. (2009, 2011).

Obviously changes in the defect structure of the implanted area under annealing are due to the diffusion of point defects and their reactions with each other and with extended defects. Though samples with $x \approx 0.2$ studied by Izhnin et al. (2019) were doped with indium while samples studied in this work were un-doped, one could not expect any effect of very moderate indium doping ($\sim 5 \cdot 10^{15}$ cm^{-3}) on the diffusion of vacancies and interstitial atoms in MCT. At the same time, Izhnin et al. (2019) suggested that the diffusion in samples with $x \approx 0.2$, which caused the upward shift of the defect layer, was strongly affected by the built-in electric field of the graded-gap surface layer, whose composition ($x=0.46$) was much larger than that of the 'active' layer of the films ($x=0.22$). In this work, this difference was much lower ($x=0.30$ and $x=0.45$, respectively), so the graded-gap layer should have affected the diffusion to a smaller extent, as the larger the composition gradient, the stronger its effect on the migration of charged defects via arising potential difference (Bogoboyashchyy et al. 2006). In this respect, TEM studies of samples similar to sample 1, which possessed a strong composition gradient at the surface, yet with a better quality of the surface of the as-grown films, should represent an interest.

Conclusion

In conclusion, we applied optical reflectance and bright-field and high-resolution transmission electron microscopy for the studies of radiation damage and formation of nano-size defect layers caused by implantation of As^+ ions with 190 keV and 350 keV energy and 10^{14} cm^{-2} fluence in MBE-grown $Hg_{0.7}Cd_{0.3}Te$ films. We observed a similarity in defect pattern formed by the implantation in $Hg_{1-x}Cd_xTe$ with $x \approx 0.2$ and $x \approx 0.3$ straight after the treatment with three nano-size defect sub-layers found in the damaged area. Defects observed in these layers were large and small dislocation loops of vacancy- and interstitial-types, single dislocations and lattice deformations. After post-implantation arsenic activation annealing, most of these defects

in $Hg_{0.7}Cd_{0.3}Te$ films, in contrast to $Hg_{0.8}Cd_{0.2}Te$ films, disappeared. This phenomenon can be tentatively related to the reduced (in contrast to $Hg_{0.8}Cd_{0.2}Te$) effect of the electric field of the graded-gap surface layer on the diffusion of charged point defects under annealing in the studied $Hg_{0.7}Cd_{0.3}Te$ films.

Compliance with ethical standards

Conflict of interest On behalf of all authors, the corresponding author states that there is no conflict of interest.

References

Bazovkin VM, Dvoretsky SA, Guzev AA et al (2016) High operating temperature SWIR p(+)–n FPA based on MBE-grown HgCdTe/Si(013). Infr Phys Technol 76:72–74

Bogoboyashchyy VV, Izhnin II, Mynbaev KD (2006) The nature of compositional dependence of p–n junction depth in ion–milled p–HgCdTe. Semicond Sci Technol 21:116–123

Bommena R, Ketharanathan S, Wijewarnasuriya PS et al (2015) High-performance MWIR HgCdTe on Si substrate focal plane array development. J Electron Mater 44:3151–3156

Bonchyk OYu, Savytskyy HV, Swiatek Z et al (2019) Nano-size defects in arsenic-implanted HgCdTe films: a HRTEM study. Appl Nanosci 9:725–730

Dvoretsky SA, Mikhailov NN, Remesnik VG et al (1998) Using reflection spectroscopy for assessing structural perfection of CdTe/GaAs films and $Cd_xHg_{1-x}Te$ crystals. Avtometriya 5:73–77 **(in Russian)**

Gravrand O, Mollard L, Largeron C et al (2009) Study of LWIR and VLWIR focal plane array developments: comparison between p-on-n and different n-on-p technologies on LPE HgCdTe. J Electron Mater 38:1733–1740

Guinedor P, Brunner A, Rubaldo L et al (2019) Low-frequency noises and DLTS studies in HgCdTe MWIR photodiodes. J Electron Mater 48:6113–6117

Izhnin II, Fitsych OI, Świątek Z et al (2019) Effect of annealing on the structural properties of arsenic-implanted mercury cadmium telluride. Opto-Electron Review 27:14–18

Koppel P (1985) Visible and ultraviolet reflectivity of $Hg_{1-x}Cd_xTe$. J Appl Phys 57:1705–1709

Lobre C, Jouneau PH, Mollard L et al (2014) Characterization of the microstructure of HgCdTe with p-type doping. J Electron Mater 43:2908–2914

Mollard L, Destefanis G, Baier N et al (2009) Planar p-on-n HgCdTe FPAs by arsenic ion implantation. J Electron Mater 38:1805–1813

Mollard L, Destefanis G, Bourgeois G et al (2011) Status of *p*-on-*n* arsenic-implanted HgCdTe technologies. J Electron Mater 40:1830–1839

Mollard L, Bourgeois G, Lobre C et al (2014) p-on-n HgCdTe infrared focal-plane arrays: from short-wave to very-long-wave Infrared. J Electron Mater 42:802–807

Park JH, Pepping J, Mukhortova A et al (2016) Development of high-performance eSWIR HgCdTe-based focal-plane arrays on silicon substrates. J Electron Mater 45:4620–4625

Shi CZ, Lin C, Wei Y et al (2016) Barrier layer induced channeling effect of As ion implantation in HgCdTe and its influences on electrical properties of p–n junctions. Appl Opt 55:D101–D105

Varavin VS, Vasiliev VV, Dvoretsky SA et al (2003) HgCdTe on GaAs: growth and devices. Opto-Electron Review 11:99–111

Yakushev MV, Brunev DV, Varavin VS et al (2011) HgCdTe heterostructures on Si(310) substrates for MWIR infrared photodetectors. Semiconductors 45:385–391

Publisher's Note Springer Nature remains neutral with regard to jurisdictional claims in published maps and institutional affiliations.